The Cryosphere
Discussions

Basal Water Storage Variations beneath Antarctic Ice Sheet Inferred from Multi-source Satellite Data

Jingyu Kang[1,2], Yang Lu[1], Yan Li[1,2], Zizhan Zhang[1] and Hongling Shi[1]

[1]State Key Laboratory of Geodesy and Earth's Dynamics, Innovation Academy for Precision Measurement Science and Technology, Wuhan 430071, China.
[2]University of Chinese Academy of Sciences, Beijing 100049, China

Correspondence to: Jingyu Kang (kangjingyu17@mails.ucas.ac.cn)

Abstract Antarctic basal water storage variations (BWSV) refer to the mass variations of liquid water beneath Antarctic ice sheet. Identifying these variations is critical to understand the behaviour of ice sheet, yet it is rarely accessible to direct observation. We presented a layered gravity density forward/inversion method for estimating Antarctic BWSV from multi-source satellite observation data, and relevant models. Results reveal spatial variability of BWSV with the mean rate of 43±13 Gt/yr during 2003-2009, which is 21 Gt/yr lower than basal melting rate. This indicates that the basal meltwater beneath Antarctic ice sheet is decreasing with the rate of -21±13 Gt/yr, accounting for 28% of the mass balance rate (-76 Gt/yr, Shepherd et al. (2018)), and the basal water migrations between basal drainage systems and oceans is non-ignorable in estimating basal mass balance of Antarctic ice sheet. Similar spatial distribution of basal water increases regions and locations of active subglacial lakes indicates that basal water storage in most active subglacial lakes is increasing. In most region of Antarctic ice sheet except Amundsen Sea coast region, the comparison of spatial BWSV and ice velocity displays a positive correlation between considerable basal water increases and rapid/accelerated ice flows, which indicates that BWSV appear to have an important effect on ice flows. Accordingly, we infer that further enhanced flow velocities are expected if basal water continues to increase in these regions.

1. Introduction

Antarctic basal water is widely generated by geothermal heating, basal pressure melting and frictional heating. The basal liquid water converge on subglacial lakes or spread over ice-bed interface, and connected to each other (Wingham et al., 2006;Fricker et al., 2016), which forms basal drainage systems with complex basal water migrations (Pattyn, 2008;Carter et al., 2015). Temporal mass variations in Antarctic basal liquid water storage are called basal water storage variations (BWSV), it influences basal effective pressure and trigger changing ice sheet velocities (Bell and Robin, 2008;Fricker et al., 2007;Alley, 1992).

BWSV are mainly controlled by basal melting rate and basal water migrations. In ice-bed interface, basal ice melt in high basal melting rate regions to increase liquid water storage, the liquid water refreezes when flowing through supercooling regions to

30 reduce the storage, besides, basal water migrations between basal drainage systems and oceans also influence spatial basal water storage variation. To date, many studies have been conducted on Antarctic basal condition (Alley et al., 1998;Rignot and Jacobs, 2002;Augustin et al., 2007;Fisher et al., 2015;Martos et al., 2017;Liefferinge et al., 2018), particularly, Pattyn (2010) inferred the Antarctic basal melting rate using a hybrid ice sheet/ice streams model. Consequently, a key question in exploring BWSV is to evaluate the basal mass balance (BMB) that is mainly caused by basal water migrations.

35 Although studies have been performed on the surface ice sheet and ice shelves, BMB over the ice sheet remains poorly understood due to limited observation. The commonly adopted approach is to examine the local surface height variations provided by altimetry observations, by assuming surface height variations related to subglacial lakes discharge (Flament et al., 2014;Wingham et al., 2006). However, this method may be invalid if BMB occurs in regions without sufficient surface expressions or with complex basal conditions, such as the Siple Coast (Young et al., 2016). Göeller et al. (2012) proposed a

40 balanced water layer concept in large scale ice sheet models to present BMB, while the modelled results depend largely on the reliability of data for building models.

In this paper, gravity variations over Antarctic ice sheet (AIS) are considered as a combination of the gravity variations caused by surface mass redistribution, basal mass balance (BMB), glacial isostatic adjustment (GIA), and ice sheet's vertical movement. We adopted an elaborate gravity forward modelling and surface density discrimination method in combination

45 with Gravity Recovery and Climate Experiment (GRACE) data, ICESat data, GPS data, and relevant models to separate the initial gravity variations caused by BMB, and employed a layered gravity density inversion method was to estimate the equivalent water height (EWH) of BMB. Afterward, the EWH of BMB was used to recalculate the gravity variation caused by surface mass redistribution and ice sheet's vertical movement, by assuming that BMB can be expressed on surface height variation, until the BMB result is stable. Finally, we combined BMB with basal melting rate data to evaluate BWSV. The

50 results were verified and interpreted based on existing research.

2. Methods

2.1 Temporal variations in gravity field and surface height on Antarctic ice sheet

Active mass redistributions on Antarctic ice sheet (AIS) occur mainly in the surface of ice sheet, ice-bed interface, and solid Earth (Fig. 1). In the surface of AIS, mass redistributions are dominated by firn layer's processes of snow accumulation,

55 sublimation/runoff, melting and firn compaction (Ligtenberg, 2014), and ice flows. In ice-bed interface, mass redistributions refer to basal mass balance (BMB) that is mainly caused by basal water migrations between basal drainage systems and oceans. Mass redistributions of solid Earth mainly refer to glacial isostatic adjustment (GIA) that describes Earth's isostatic deformation since the last glacial stage, such as mantle convection, and Earth's load deformation caused by load of the overlying ice sheet.

60 Mass redistributions lead to temporal variations in gravity field defined in geoid, and can be captured by Gravity Recovery
and Climate Experiment (GRACE) observations. These variations contain surface gravity variations caused by snow
accumulation, sublimation/runoff and ice flow, gravity variations of BMB in ice-bed interface, and gravity variations of solid
Earth that arise from the combined effect of GIA and Earth's load deformation. Besides, BMB and basal melting/refreezing
also influence ice sheet's vertical movement by controlling basal mass changes and ice-water phase change process, thereby

65 contributing to gravity variations. Accordingly, we can express the Antarctic integrated time-variable gravity field as a
superposition of layered gravity variations:

$$\Delta dg_{GRACE} = \Delta dg_{surf} + \Delta dg_{BMB} + \Delta dg_{GIA} + \Delta dg_{IVM} \tag{1}$$

where Δdg_{GRACE} are Antarctic integrated time-variable gravity variations (including load effect) observed by GRACE (section
3.1); Δdg_{surf} are gravity variations caused by Antarctic surface mass redistributions process, including firn layer's processes

70 and ice flow; Δdg_{BMB} are BMB-derived gravity variations; Δdg_{GIA} are gravity variations caused by Earth's isostatic
deformation and mass changes in the interior of the Earth, and can be obtained from GIA model (section 3.4); Δdg_{IVM} are
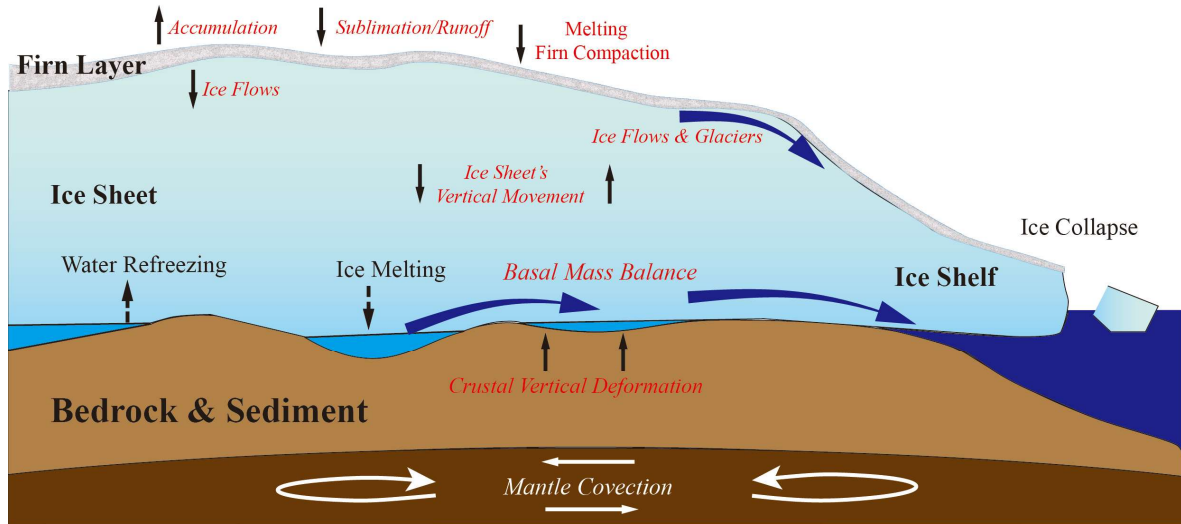additional gravity variation caused by ice sheet's vertical movement.

Figure 1 Mass redistributions in different layers on AIS. Italics are components that contribute to gravity variations, and
red fonts refer to components resulting in surface height variations. Ice sheet's vertical movement is controlled by combined
effect of BMB, basal water refreezing and ice melting. Crustal vertical deformation refers to Earth's isostatic and load
deformation.

Mass redistributions also lead to surface height variations of AIS:

$$dh_{ICESat} = dh_{FL} + dh_{IF} + dh_{IVM} + dh_{CVD} \tag{2}$$

75 where dh_{ICESat} are AIS surface height variations that can be observed by ICESat (section 3.2); dh_{FL} are height variations
caused by process of firn layer including surface snow accumulation, sublimation/runoff, melting and firn compaction. dh_{IF}

3

are height variations caused by ice flow; dh_{IVM} are the ice sheet's vertical movement; dh_{CVD} are crustal vertical deformations that be calculated by fitting GIA predicted basal uplift rate to sparse GPS observation rate (section 3.4).

2.2 Estimation of basal mass balance and basal water storage variations

80 Separation of Δdg_{BMB} from integrated time-variable gravity field (Equation 3) is enabled by different sensitivity of satellite observation with respect to gravity and height variations in different layers. According to Equation 1, Δdg_{BMB} can be expressed as follows:

$$\Delta dg_{BMB} = \Delta dg_{GRACE} - \Delta dg_{surf} - \Delta dg_{GIA} - \Delta dg_{IMV} \tag{3}$$

In Equation 3, Δdg_{surf} and Δdg_{IVM} can be calculated through gravity forward modelling method and corresponding density
85 data, providing the known height variations caused by surface process and ice sheet's vertical movement. Then mass changes of BMB can be estimated from Δdg_{BMB} by utilizing gravity density inversion method. However, height variations caused by surface process are complicated, especially in ice flow regions where the surface height variations are dominated by ice thinning, and the combination of surface and ice density is more appropriate in gravity forward modelling process; furthermore, BMB and basal melting/refreezing cause ice sheet's vertical movement, and this movement is also expressed as height
90 variations and result in additional gravity variation Δdg_{IVM}. These coupled variations are contained in gravity and surface height variations that captured by satellite gravity and altimetry mission. Therefore, the key problem of separating dg_{BMB} from integrated time-variable gravity field is to distinguish different height variation components on each layer and IVM from altimetry observation data. For this purpose, we adopted an iteration method that accounts for surface density discrimination and IVM correction, to estimate the corresponding height and gravity variation (Fig. 2), details are described as follows.

95 Firstly, we set the initial value of dh_{IVM} to 0, and deducted dh_{CVD} and dh_{IVM} from AIS surface height variation dh_{ICESat}, to obtain the initial height variation from Antarctic surface mass redistributions $dh_{surf} = dh_{ICESat} - dh_{IVM} - dh_{CVD}$. It is noticed that dh_{surf} only contains height variations caused by firn layer's processes dh_{FL} and ice flow dh_{IF}. Afterward, we utilized surface density discrimination method (Gunter et al., 2014), in combination with a semi-empirical estimated time-dependent firn densification model (FDM) that describes spatio-temporal evolution of Antarctic firn layer (Ligtenberg et al.,
100 2011) (section 3.3), to discriminate height variation component from dh_{surf}. The corresponding surface density ρ is assigned as follows:

$$\rho = \begin{cases} \rho_{firn}\, for\, dh_{FDM},\, \rho_{ice}\, for\, (dh_{surf} - dh_{FDM}) & if\, (dh_{surf} - dh_{FDM}) < 0\, \&\, |dh_{surf} - dh_{FDM}| > 2\sigma_{dh} \\ \rho_{surf}\, for\, dh_{surf} & if\, (dh_{surf} - dh_{FDM}) > 0\, \&\, |dh_{surf} - dh_{FDM}| > 2\sigma_{dh} \\ 0 & otherwise \end{cases} \tag{4}$$

where ρ_{firn} are firn density distributions (Ligtenberg et al., 2011); dh_{FDM} are height variations derived from FDM that provides temporal surface height variations caused by the surface mass balance variations, liquid water processes (snowmelt,

105 percolation, refreezing and runoff) and firn compaction (Ligtenberg et al., 2011). ρ_{ice} is ice density (917 kg m^{-3}) and $\sigma_{dh} = \sqrt{\delta_{ICESat}^2 + \delta_{FDM}^2}$.

As shown in Equation 4, the negative height differences between dh_{surf} and dh_{FDM} greater than $2\sigma_{dh}$ are attributed to ice flow (that is, $dh_{IF} = dh_{surf} - dh_{FDM}$) with the assignment of ice density ρ_{ice}, and surface firn density ρ_{firn} is assigned to dh_{FDM}. Similarly, positive height difference greater than $2\sigma_{dh}$ are attributed to underestimation of FDM, and surface firn

110 density ρ_{firn} is assigned to dh_{surf}. Then gravity forward modelling method (section 2.3) is employed to calculate dg_{surf} in Equation 3.

Secondly, we set initial Δdg_{IVM} to 0, and deducted initial value of Δdg_{surf}, Δdg_{GIA} and Δdg_{IVM} from Antarctic integrated time-variable gravity Δdg_{GRACE}, to obtain the initial Δdg_{BMB} in Equation 3. Then gravity inversion method (section 2.3) was used to estimate initial mass variations of BMB (Δm_{BMB}, in form of equivalent water height (EWH)), and a 300km gaussian

115 filter was performed on Δm_{BMB} to match the spatial resolution of GRACE data. Thirdly, we used basal melting rate data (section 3.5) (Pattyn, 2010) to judge whether basal is in melting or freezing condition, and combined Δm_{BMB} to calculate dh_{IVM}. The calculation of dh_{IVM} was performed based on the assumption of ice layer's instant vertical movement in response to BMB: in basal melting regions, ice sheet's vertical movement dh_{IVM} is replaced by Δm_{BMB}; in basal freezing regions, dh_{IVM} was replaced by $\Delta m_{BMB} * \rho_{ice}/1000$. The ice layer's instant response assumption is reasonable and can be justified by strong

120 surface height variations (up to 90m/yr) caused by subglacial lakes water changes in a short time (Fricker et al., 2016). Afterward, dh_{IVM} was used to calculate the gravity correction of ice sheet's vertical movement Δdg_{IVM}. Calculation of Δdg_{IVM} can be achieved by estimating gravity difference between ice sheet before and after it moves, while this correction method is multifarious due to the complication of surface process. For simplicity, we only updated the value of dh_{IVM} in first step, and repeated the surface density discrimination method for iteration, until the Δm_{BMB} is stable (with the total BMB difference

125 between two iterations smaller than 5Gt/yr). Finally, we combined Δm_{BMB} and basal melting rate data (Pattyn, 2010) to evaluate basal water storage variations (Δm_{BWSV}, in form of equivalent water height (EWH)): regions with basal melting rate greater than 0 are assumed to maintain basal water migrations, and the (Δm_{BWSV} are the gross of Δm_{BMB} and basal ice melting; regions with the melting rate of 0 are assumed to be at supercooling condition, and no BWSV occurs in these regions.
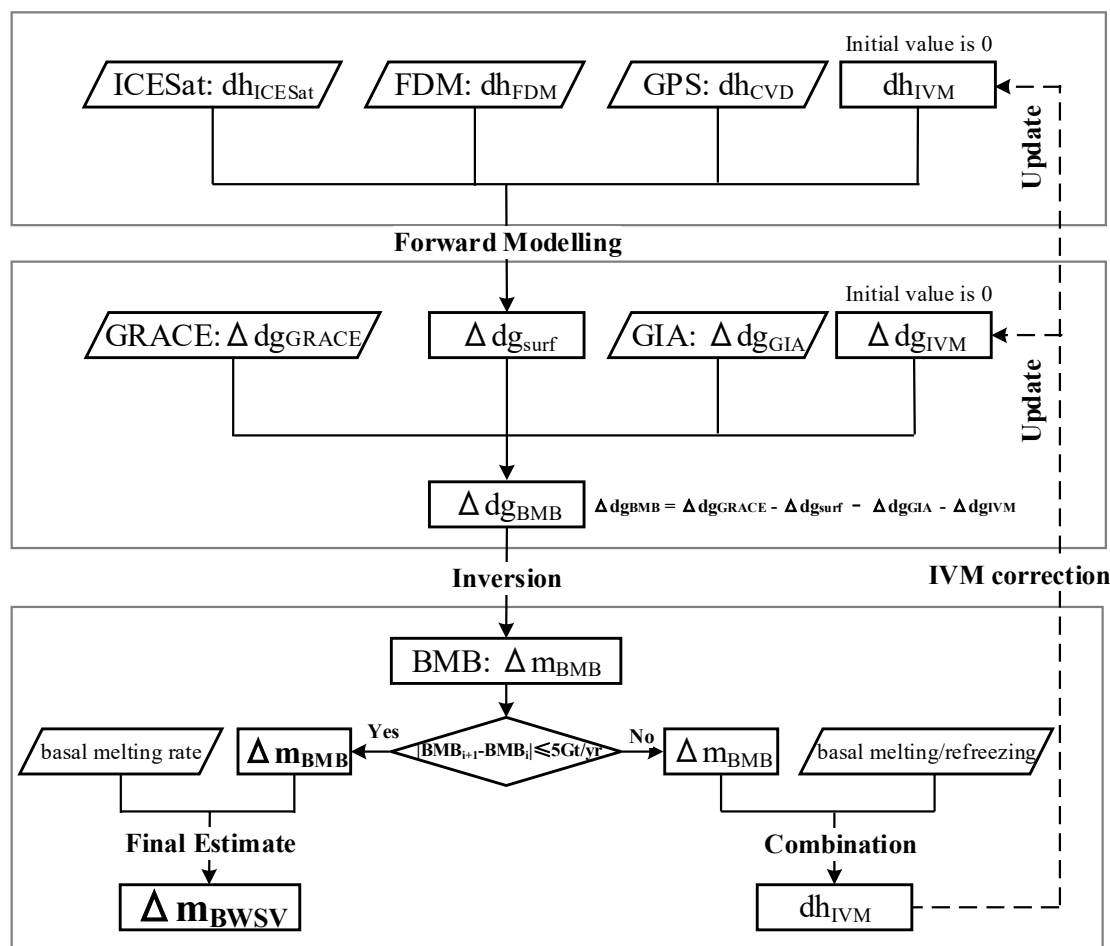
Figure 2 Flowchart for estimating basal mass balance (BMB) and basal water storage variations (BWSV). Firstly, initial values of Antarctic surface gravity variations Δdg_{surf} are calculated through gravity forward modelling method in combination with ICESat, FDM, GPS and GIA data. Secondly, BMB-derived gravity variations Δdg_{BMB} are abstracted from GRACE, and BMB are estimated through gravity density inversion method. Thirdly, ice sheet's vertical movement (IVM) are used to perform gravity correction. For simplicity, IVM is only updated in first step for iteration in order to avoid multifarious gravity correction of Δdg_{IMV}.

2.3 Gravity density inversion method based on forward modelling

130   Gravity forward modelling is used to convert the volume variations and density distribution data into gravity variations. In this study, we adopted an oblique triangular prism that addresses terrain surfaces on ellipsoids without gaps. For this purpose, surface of AIS was divided into many equilateral triangles with sides approximately 50km (Fig. 3). Gravity variations are given by the basic gravity forward modelling Equation (Hofmann-Wellenhof and Moritz, 2006):

The Cryosphere
Discussions

Open Access

$$dg = -G\rho \iiint \frac{z}{(x^2+y^2+z^2)^{3/2}} dxdydz \qquad (5)$$

135 where G is the gravitational constant, ρ are density distributions related to volume variations (section 3.3).

Volume integral in Equation 5 can be modified into surface integral, accordingly, gravity variations components in different Antarctic layers are expressed as the sum of gravity variations of oblique triangular prism:

$$dg = \sum_{k=1}^{N} G\rho_k [\iint \frac{1}{(x_k^2+y_k^2+z_{k\_l}^2)^{\frac{1}{2}}} dx_k dy_k - \iint \frac{1}{(x_k^2+y_k^2+z_{k\_u}^2)^{\frac{1}{2}}} dx_k dy_k] \qquad (6)$$

where dg are gravity variations in AIS layers that defined in geoid, N is the number of triangular prisms within the integrated

140 radius (500km), ρ_k are density of each triangular prisms, z_{k_l} and z_{k_u} are lower/upper surface height of each triangular prisms (that is, AIS's basal and surface height that comes from BEDMAP2 (Fretwell et al., 2013)).
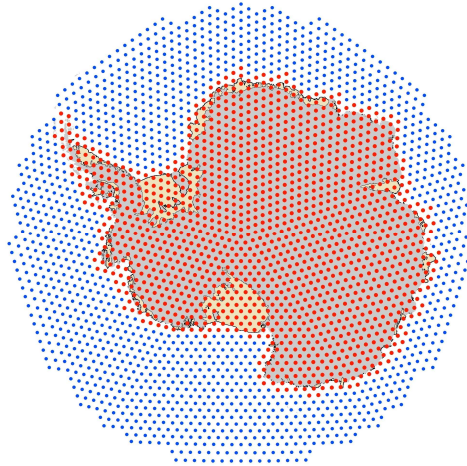

Figure 3 Vertexes of triangles used for gravity forward modelling/inversion. Grey regions are Antarctic ice sheets (AIS), yellow regions are Antarctic ice shelves. Red points are vertexes of 10314 triangles used for estimating BMB through gravity inversion method, and these triangles are extended 1° outward for reducing possible leakage-out errors of gravity signals.

Then a layered gravity density inversion method was developed to estimate BMB. In this method, BMB was assumed to occur on a thin layer in Antarctic ice-bed interface, with a fixed thickness and variable density. Then BMB induced gravity variations can be expressed as follow:

145 $$\Delta dg_{BMB} = \sum_{k=1}^{N} G\rho_k [\iint \frac{1}{(x_k^2+y_k^2+z_k^2)^{\frac{1}{2}}} dx_k dy_k - \iint \frac{1}{(x_k^2+y_k^2+(z_k+dz)^2)^{\frac{1}{2}}} dx_k dy_k] \qquad (7)$$

$$\rho_k = \rho_w H_k \qquad (8)$$

where dz is the thickness of the fixed layer on Antarctic bedrock, ρ_k is fixed thin layer's density distribution, ρ_w is water density, H_k is the EWH of BMB that need to be estimated.

Then, Equation 7 could be modified as follows:

$$\frac{\Delta dg_{BMB}}{G\rho_w} = \sum_{k=1}^{N} H_k [\iint \frac{1}{(x_k^2+y_k^2+z_k^2)^{\frac{1}{2}}} dx_k dy_k - \iint \frac{1}{(x_k^2+y_k^2+(z_k+dz)^2)^{\frac{1}{2}}} dx_k dy_k] \tag{9}$$

For M gravity points (M=10314), Equation 9 can be expressed as:

$$d = BX \tag{10}$$

where

$$d = \begin{bmatrix} \frac{\Delta dg_{BMB_1}}{G\rho_w} \\ \vdots \\ \frac{\Delta dg_{BMB_M}}{G\rho_w} \end{bmatrix}; B = \begin{bmatrix} T_{11} & \cdots & T_{1N} \\ \vdots & \ddots & \vdots \\ T_{M1} & \cdots & T_{MN} \end{bmatrix}; X = \begin{bmatrix} H_1 \\ \vdots \\ H_N \end{bmatrix};$$

$$T_{MN} = [\iint \frac{1}{(x_{mn}^2+y_{mn}^2+z_{mn}^2)^{\frac{1}{2}}} dx_{mn} dy_{mn} - \iint \frac{1}{(x_{mn}^2+y_{mn}^2+(z_{mn}+dz)^2)^{\frac{1}{2}}} dx_{mn} dy_{mn}]$$

Then the conjugate gradient method was employed to solve the EWH of BMB (that is, X in Equation 10).

2.4 Uncertainty estimation

Estimating uncertainties of BMB/BWSV is comprehensive due to the combination of multi-source data in gravity forward/inversion including GRACE, ICESat, FDM, GPS, GIA, and basal melting rate. Among them, Uncertainties of GRACE are provided by calibrated errors for spherical harmonic coefficients, and can be estimated utilizing the method of Wahr et al. (2006); Others are provided by uncertainties of volume variations or uplift rate, and can be converted to associated gravity uncertainties by using cylinder model (Heiskanen and Moritz, 1967) combined with error propagation law. The uncertainty of BMB is obtained as follows:

$$\delta\Delta dg_{BMB} = \sqrt{\delta\Delta dg_{GRACE}^2 + \delta\Delta dg_{ICESat}^2 + \delta\Delta dg_{FDM}^2 + \delta\Delta dg_{GPS}^2 + \delta\Delta dg_{GIA}^2} \tag{11}$$

where $\delta\Delta dg_{GRACE}$, $\delta\Delta dg_{ICESat}$, $\delta\Delta dg_{FDM}$, $\delta\Delta dg_{GPS}$, $\delta\Delta dg_{GIA}$ are uncertainty of gravity variations related to GRACE, ICESat, FDM, GPS and GIA respectively.

Afterward, uncertainties of BMB $\delta\Delta m_{BMB}$ are calculated from $\delta\Delta dg_{BMB}$, based on the inversion of cylinder model and error propagation law, and uncertainties of BWSV $\delta\Delta m_{BWSV}$ are estimated as follow:

$$\delta\Delta m_{BWSV} = \sqrt{\delta\Delta m_{BMB}^2 + \delta\Delta m_{BM}^2} \tag{12}$$

170   where $\delta\Delta m_{BMB}$ refers to EWH uncertainties of BMB, $\delta\Delta m_{BM}$ refers to standard deviations of basal melting rate (Pattyn, 2010;Van Liefferinge and Pattyn, 2013).

3.   Data processing

3.1   Time-varying gravity data derived from GRACE

Time-varying gravity data comes from three Release 06 (RL06) monthly GRACE gravity field solutions provided by the

175   University of Texas Center for Space Research (CSR), the Jet Propulsion Laboratory (JPL), and the German Research Centre for Geosciences (GFZ). Each solution is represented by fully normalized Stokes potential coefficients with degree and order to 60. The C20 coefficients of each GRACE solution were replaced by satellite laser ranging (Cheng et al., 2013), and the degree 1 coefficients are inserted by the values of Swenson et al. (2008). Striping errors were eliminated by using P4M6 filter (Chen et al., 2007) and 300km Gaussian smoothing filter. Scaling factors was multiplied to restore the amplitude dampening

180   and leakage-out errors (Gao et al., 2015). In this study, basal mass balance signals contained in GRACE only occurs in AIS region, so leakage-in errors corrections were not performed here. Linear term was abstracted through least squares adjustment of six-parameter function consisting of constant term, linear trend, annual and semi-annual periodic signals. The gravity variation trend was calculated according to the spherical-harmonic expansion of the gravity anomaly (Heiskanen and Moritz, 1967) (Equation 13), and we used the mean gravity variations trend from the three GRACE solutions to account for time-

185   varying gravity on AIS. It is worth noting that time-varying gravity contains not only linear trend of AIS gravity variations, but also load effect. Then the AIS time-varying gravity trend dg_{GRACE} is expressed as follows:

$$\Delta dg_{GRACE} = \frac{GM}{R^2}\sum_{n=2}^{max}(n-1)\frac{1}{1+k_n}\sum_{m=0}^{n}\bar{P}_{nm}(cos(\theta))[\Delta C_{nm}\,cos(m\phi) + \Delta S_{nm}\,sin(m\phi)] \tag{13}$$

where GM is the geocentric gravitational constant, R is the mean radius of Earth, k_n is the load Love number of degree n (Wahr et al., 1998), $\bar{P}_{nm}$ are the normalized associated Legendre functions, ΔC_{nm} and ΔS_{nm} are modified harmonic

190   coefficients, θ and ϕ are colatitude and longitude, and $r(\theta)$ is the geocentric distance related to θ.

The uncertainties were estimated through the method of Wahr et al. (2006), from the calibrated errors for spherical harmonic coefficients provided by CSR, JPL and GFZ, and coefficient errors of degree 1 and degree 2 were replaced by the corresponding standard deviations provided by Cheng and Swenson (Cheng et al., 2013;Swenson et al., 2008). Figure 4a-4f show linear trend and corresponding uncertainties of AIS gravity variations respected to three GRACE solutions over the

195   period between February 2003 and October 2009, which is consistent with the ICESat simultaneously observation period in order to avoid sampling effects. All figures of AIS region are shown in Antarctic polar stereographic projection coordinates.
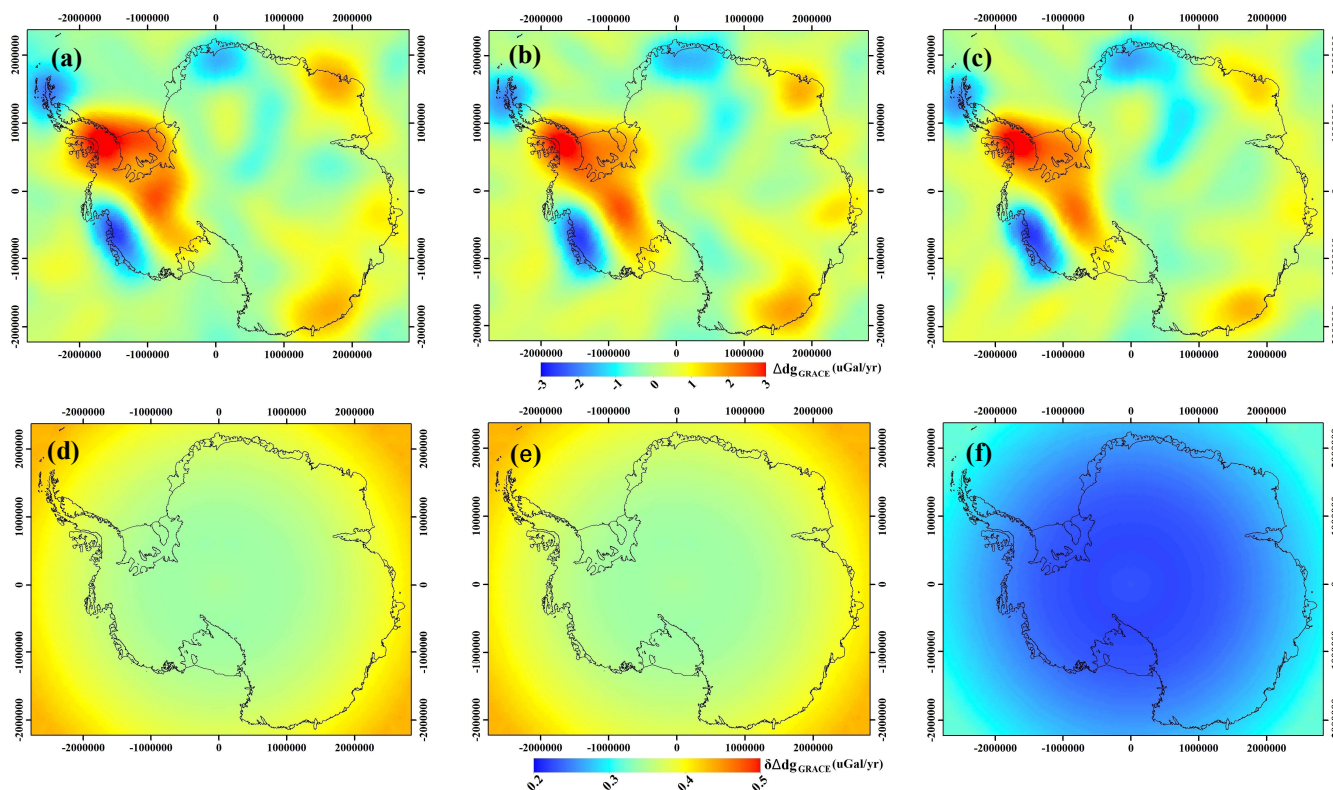
Figure 4 Linear trend of AIS gravity variations estimated from **(a)** CSR **(b)** JPL and **(c)** GFZ solutions, and **(d)**, **(e)**, **(f)** associated uncertainties in unit of uGal/yr. These monthly solutions during 2003–2009 are consistent with the ICESat mission time.

3.2 Surface height variations derived from ICESat

Height variations on surface AIS were derived from Ice, Cloud, and Land Elevation Satellite (ICESat) mission, which were provided by National Snow and Ice Data Center (NSIDC), with the mission period spanning from February 2003 to October

200 2009. The object of ICESat mission is to obtain the height variations with an accuracy of ≤1.5cm/yr for spatial resolution of $100*100km^2$ on AIS (Zwally et al., 2002). Therefore, we estimated AIS height variations by using a block crossover analysis method (Brenner et al., 2007;Gunter et al., 2009) with each block size about $100*100 km^2$. In pre-processing of ICESat data, crossover points with height variations greater than 10m/yr were deleted in order to eliminate gross errors caused by the small-scale surface roughness, undetected forward scattering and the interpolation between successive footprints, then the 3σ

205 criterion test was carried out in each block area to further eliminate the residual gross errors (Smith et al., 2005). The linear surface height variations trends were abstracted through least squares adjustment of four-parameter function consisting of constant term, linear trend, and annual periodic signals.

The inter-campaign biases (ICB) have been evaluated by several research groups through a variety of approaches, while these ICB corrections vary largely due to the selection of different reference surfaces. Zwally et al. (2015) made the correction by

210 using concurrent Envisat radar altimetry of the same surface in open water and thin ice in leads and polynyas in Antarctic sea
ice pack. Richter et al. (2014) and Schroeder et al. (2016) made the correction based on a near-zero surface height changes and
hydrostatic equilibrium for the snow surface above Lake Vostok and its surroundings in East Antarctica (EA) that is concluded
by repeat measurement of a GPS stake network and kinematic profile resurveys. Other methods for ICB estimations are
performed based on the assumption of near-zero elevation changes regions in EA. To date, none of ICB corrections has been

215 endorsed by the ICESat Science Team, NASA, or NSIDC. Therefore, uncertainties of ICB corrections also have an evident
influence on the estimation of BMB results. In this study, we used the mean ICB corrections value of Zwally et al. (2015),
Richter et al. (2014) and Schroeder et al. (2016), to avoid the artificial near-zero elevation changes assumption.

Figure 5a shows linear trend of AIS surface height variations (including ICB corrections), with the grid size of 100*100 km^2.
Figure 5b shows the uncertainties of mean height variations trend. To match with the GRACE spatial resolution, a 300km

220 Gaussian smoothing filter was performed in the surface height variations before calculating surface gravity variations.
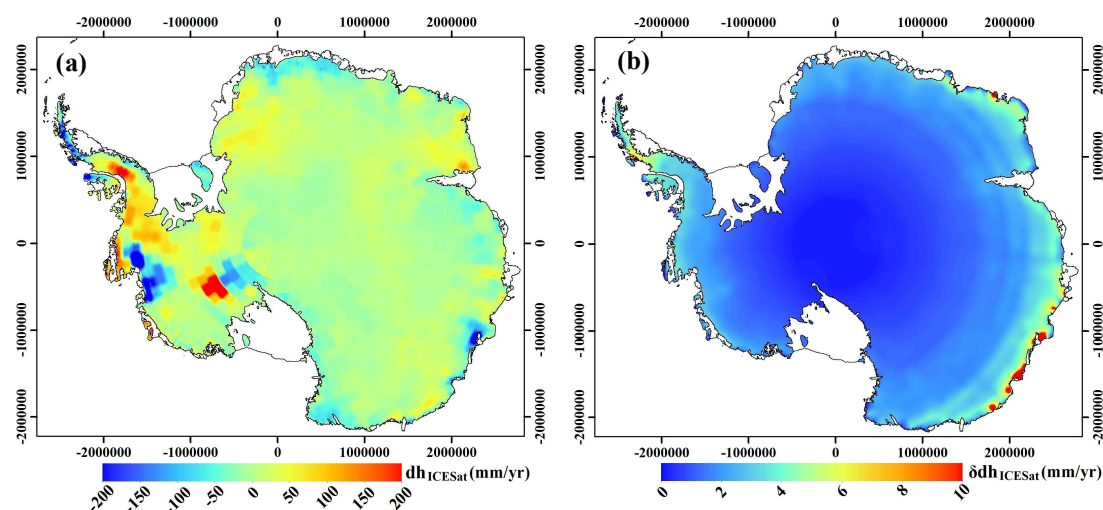

Figure 5 (a) Linear surface height variations trend (including ICB corrections) during February 2003 - October
2009 (truncated at 200 mm/y). **(b)** Associated uncertainties of height variation trend.

3.3 Firn densification model

Height variations of AIS firn layer are associated with both mass-conserving (firn compaction), mass-changing (snow
accumulation, sublimation/runoff) processes, and ice flow (Zwally et al., 2005;Gunter et al., 2014). Mass-conserving process
only influences surface height variation, and have no effect on gravity variation. Therefore, discriminating these processes is

225 essential for estimating volume variations from firn layer's mass-changing and ice flow, thereby contributing to converting
surface volume variations into gravity variations in combination of surface density distribution of Kaspers et al. (2004). For
this purpose, the Institute for Marine and Atmospheric Research Utrecht Firn Densification Model (IMAU-FDM) (Ligtenberg

et al., 2011) was used to account for height variations caused by firn layer's process. IMAU-FDM is presented by an improved firn densification expression that is tuned to fit depth-density observation and liquid water processes (meltwater percolation,

230   refreezing and retention). At AIS surface, the time-dependent IMAU-FDM is forced by the surface mass balance, surface temperature and wind speed from the regional atmospheric climate model RACMO2/ANT, to simulate the temporal evolution of firn density and surface height (Ligtenberg et al., 2011). For simplifying calculation process, this study used a constant surface firn density model from IMAU-FDM, which would cause a mean bias of -20.4kg m^{-3} compared with the temporal firn density (Keenan et al., 2021), while this bias is negligible compared with the mean density of 340kg m^{-3} over AIS. Figure 6a-

235   6b shows the linear surface height changes rate derived from IAMU-FDM and the associated uncertainties over the study period. For the consistency of spatial resolution, a 300km Gaussian filter was also performed in IAMU-FDM-derived surface height changes rate.
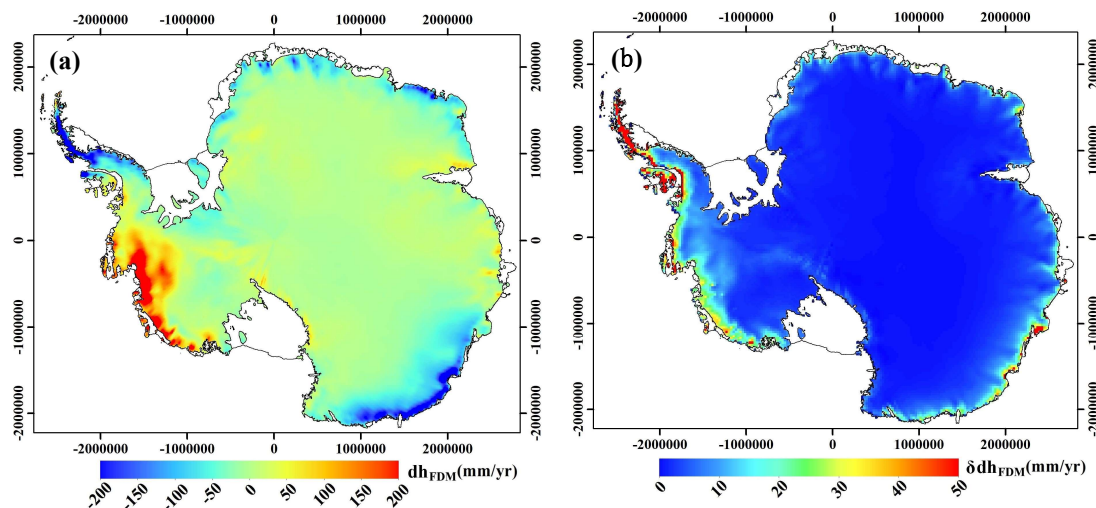

Figure 6 (a) Linear trend of firn layer's height variations derived from IAMU-FDM over the study period and

(b) associated uncertainties

3.4   Glacial isostatic adjustment and crustal vertical deformation rate derived from GPS

In our study, three GIA models were used to account for Earth's isostatic deformation and mass changes in the interior of the

240   Earth, including ICE-6G (Peltier et al., 2015;Argus et al., 2014), IJ05_R2 (Ivins et al., 2013) and W12a (Whitehouse et al., 2012). ICE-6G is a global GIA modal that is constrained to fit all available geological and geodetic observation data including GPS, ice thickness, relative sea level histories and the age of marine sedimentation. IJ05_R2 and W12a are regional GIA models that are constrained by extensive geological and glaciological data. All GIA model provides geoid rate in form of stokes coefficients, as well as predicated uplift rate in grid format. Uncertainties of ICE-6G and IJ05_R2 arise from the misfit

245   between uplift rates from GIA and GPS: for ICE-6G, the rms value of 0.89 mm/y is estimated from 42 GPS stations (Argus et

al., 2014); for IJ05_R2, the uniform value of 1.40 mm/y comes from 6 GPS stations with observation period over 3000 days (Ivins et al., 2013). Uncertainty of W12a is provided by the upper and lower bounds of geoid rates.

The crustal vertical deformation rate on Antarctica contains two components: Earth's isostatic deformation and load deformation of the crust due to the mass changes of ice sheet. The combined deformation rate during 1995-2013 comes from

250 GPS observed uplift rates from a total of 118 GPS sites listed in Sasgen et al. (2016). We used 57 of them over the study period, and removed sites with the errors greater than uplift rates. The sparse GPS data were interpolated by the GIA predicated spatial uplift distribution, to obtain the crustal vertical deformation throughout the whole Antarctic ice sheet. Figure 7a-7c shows the predicated uplift rate derived from ICE-6G, IJ05_R2 and W12a, as well as the uplift rate and their uncertainties of 57 GPS sites.
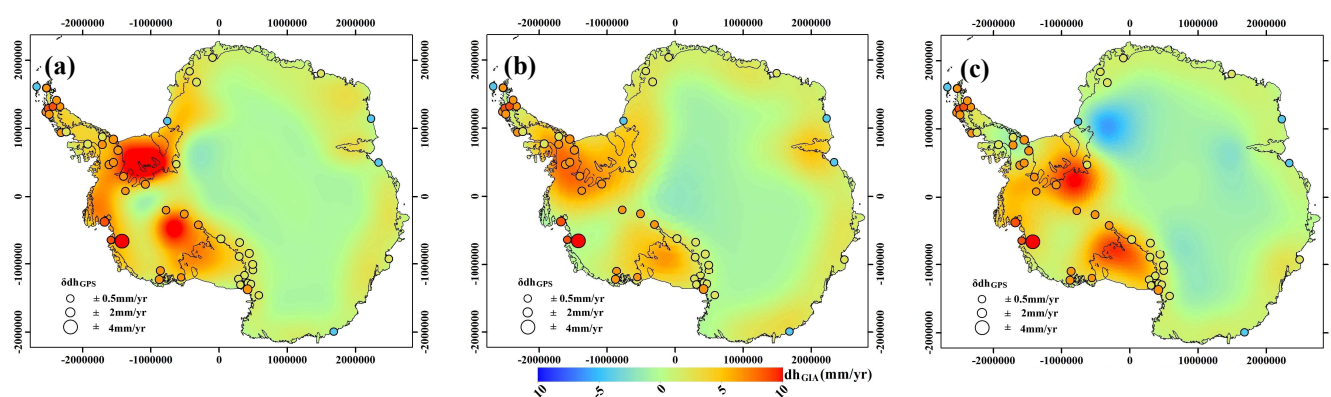

Figure 7 GIA predicated uplift rate from **(a)** ICE-6G, **(b)** IJ05_R2, **(c)** W12a. And GPS observations for crustal vertical deformation rate and associated uncertainties during 2003-2009. The color of the circle donates the uplift rate and radius donates the uncertainties.

255 **3.5 Basal melting rate**

Antarctic basal melting rate was used to estimate basal water storage variations (BWSV) in combination with basal mass balance (BMB). The basal melting data used in this study is determined by Pattyn (2010), through a hybrid method that combines a priori information (such as on-site measurements data), topography, accumulation, surface temperature, geothermal heat flow data with a merged ice sheet/ice stream model. The associated uncertainty is evaluated through a series

260 of sensitivity experiments. The multi-source dataset used in estimating basal melting rate cover different period spanning from 1980 to 2004 (Pattyn, 2010;Van Liefferinge and Pattyn, 2013), differing from the period of this study (2003-2009). Nevertheless, this period discrepancy has little influence on our estimation of BWSV, due to the stable basal conditions caused by isolation of overlying ice sheet.

Figure 8a-8b shows the mean basal melting rate and the standard deviation for sensitivity experiments. Where the highest melt

265 rates are situated in West Antarctica (WA), while freezing regions are associated with subglacial mountain ranges with overlying thin ice, and the surrounding of EA. The mean basal melting rate of AIS is 5.3 mm/y, which lead to a total basal

water mass change rate of 65 Gt/y. In this study, we used a 300km Gaussian smoothing filter on the basal melting rate to match the spatial resolution of BMB.
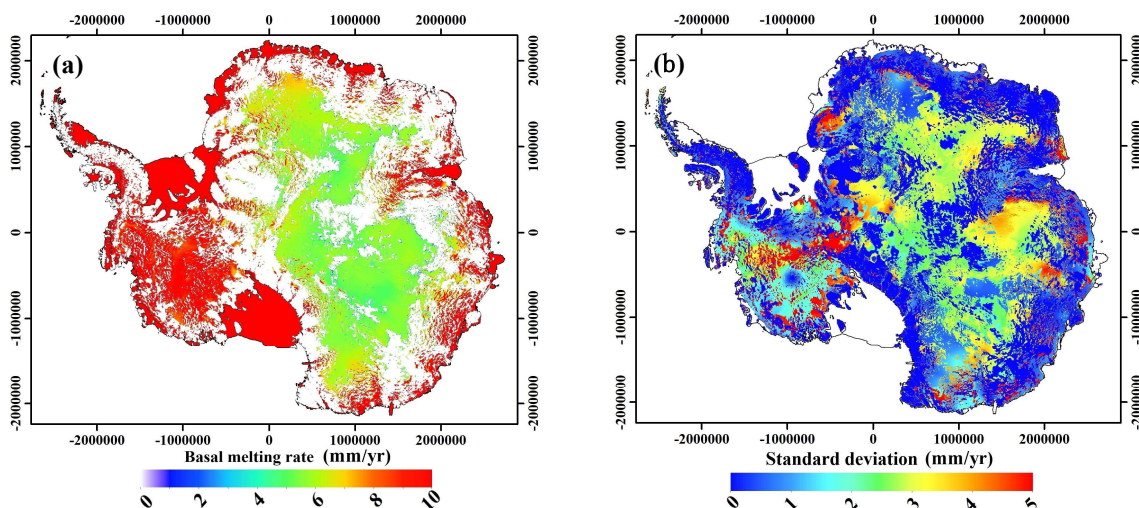

Figure 8 (a) Basal melting rate on Antarctic ice sheet (truncated at 10 mm/y) and **(b)** associated standard deviation. These datasets come from Pattyn (2010).

4. Results and discussion

4.1 Basal mass balance beneath Antarctic ice sheet

Based on the gravity density forward/inversion iteration method in section 2.2, we calculated the Antarctic basal mass balance (BMB) that is mainly caused by basal water migrations. Figure 9 displays the BMB result for each iteration related to 3 glacial isostatic adjustment (GIA) models. As shown in figure 9, three BMB results all converge to stable negative value in the seventh iteration, indicating the total basal mass balance of AIS in continuously decreasing during 2003-2009. Total BMB results related to ICE-6G and W12a show consistent greater variations in the first iteration and converge to a large value (~-20Gt/yr), while the BMB result related to IJ05_R2 shows a relatively small value.
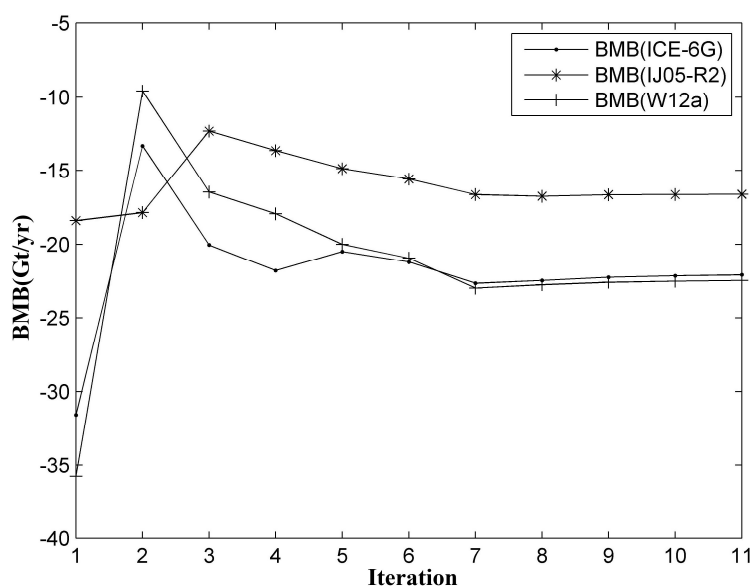
Figure 9 Total basal mass balance (BMB) results on Antarctic ice sheet for
each iteration (in unit of Gt/yr).

Regional BMB rates related to 3 GIA models based on 18 drainage basins from Rignot et al. (2019) (shown in Figure 10a-10c)
and associated standard deviations are shown in Table 1. The drainage basins division method is employed based on the spatial
similarity of simulated basal meltwater pathways and surface ice flows. As shown in Table 1, although different GIA models

280 are used in estimating BMB, regional BMB rates related to 3 GIA models show similar values in most of the drainage basins:
3 drainage basins (B5, B6 and B9) exhibit obvious basal mass increases (with the absolute value of regional BMB rates greater
than associated standard deviations and lager than 10Gt/yr), and 3 drainage basins (B2, B3 and B11) displays obvious basal
mass decreases. Mean BMB rates (average of BMB rates related to 3 GIA models) in East Antarctic Ice Sheet (EAIS, including
B1-B8, B17 and B18) and West Antarctic Ice Sheet (WAIS, including B9-B12 and B16) are 11 ± 12 Gt/yr and -31 ± 5 Gt/yr,

285 accounting for 23% and 30% of the corresponding ice-sheet mass balance estimated by satellite gravimetry method (Shepherd
et al., 2018), respectively. Mean BMB rate in Antarctic Peninsula Ice Sheet (APIS, including B13-B15) is very low (-1 ± 1
Gt/yr), indicating that there are few basal mass variations. The total mean BMB rate beneath Antarctic Ice Sheet (AIS) is -21
± 13 Gt/yr, accounting for 28% of the satellite gravimetry derived ice-sheet mass balance rate (-76Gt/yr) from Shepherd et al.
(2018).

290 Figure 10 displays spatial distributions of BMB trend on AIS related to 3 GIA models, and associated standard deviations
(STD), in form of equivalent water height (EWH). In Figure 10a-10c, red colours represent basal mass increases regions where
the input volume of basal mass is greater than the output volume; blue colours represent regions with basal mass decreases;
the dash regions are where the BMB rates are less than the STD, that is, BMB result is not significant in these regions. Figure
10a-10c shows similarly spatial distributions of BMB trend that related to 3 GIA models: where basal mass variations occur

295 mainly in WAIS, marginal regions of EAIS and Wilkes Land. The associated STD (Figure 10d-10f) also shows consistent spatial distributions: the largest STD (≥15 mm/yr) are in APIS and WAIS, which mainly comes from the STD of GRACE (about 25% of total STD estimated from Equation 11), ICESat (25%, mainly from ICB), FDM (20%) and GPS (20%); the medium STD (10-15 mm/yr) are in the marginal region of EAIS, mainly coming from GRACE (40%), ICESat (30%) and FDM (20%); the low STD (<10 mm/yr) cover a large extent the interior of EAIS, mainly coming from GRACE (45%) and
300 ICESat (35%).

Table 1 Regional Antarctic basal mass balance (BMB) rates related to 3 GIA models in 18 drainage basins
and associated standard deviations, in unit of Gt/yr

Basin	BMB(ICE-6G)		BMB(IJ05_R2)		BMB(W12a)		Basin	BMB(ICE-6G)		BMB(IJ05_R2)		BMB(W12a)	
	Rates	Std	Rates	Std	Rates	Std		Rates	Std	Rates	Std	Rates	Std
B1	4	4	4	5	4	4	B11	-41	3	-40	4	-45	3
B2	-10	4	-11	4	-11	3	B12	-1	1	-1	1	-1	1
B3	-10	7	-9	9	-11	7	B13	0	1	0	1	-1	1
B4	-1	4	-1	5	-1	4	B14	1	1	1	1	1	1
B5	20	7	21	8	20	7	B15	-2	1	-2	1	-2	1
B6	12	4	11	5	12	4	B16	4	4	2	5	0	4
B7	2	2	1	2	2	2	B17	0	12	0	13	3	11
B8	-6	9	-8	10	-4	8	B18	0	2	0	2	0	2
B9	9	5	18	6	15	5							
B10	-4	1	-4	1	-4	1	Total	-23	21	-18	24	-22	20

In Figure 10a-10c, significant basal mass increases (with the BMB rates greater than associated standard deviations) occur mainly in Rockefeller Plateau (RP), Siple Coast (SC), George V Coast (GVC), Aurora Subglacial Basin (ASB), marginal area
305 of Dronning Maud Land (DML), Slessor Glacier (SG), Recovery Ice Stream (RIS) and Institute Ice Stream (IIS). Among them, RP, SC, GVC and ASB region possess the most obvious basal mass increases, this is attributed to the low-lying basal terrain facilitating the accumulation of basal meltwater driven by basal hydraulic potential gradient (Fig 18, (Göeller, 2014)), and Wright et al. (2012) revealed the possibility of basal meltwater accumulation in ASB region by revealing extensively distributed basal pressure melting through regional airborne geophysical survey and numerical ice sheet modelling method. In
310 SC region, the mechanism of basal meltwater accumulation is also revealed in MacAyeal and Whillans ice streams, where the similar basal hydrological systems are also found (Fricker et al., 2016;Gray et al., 2005); additionally, the accumulated basal meltwater in SC region might also partially account for the dynamic thickening of Kamb ice stream. Similarly, basal mass increases in IIS regions should be also caused by low basal hydraulic potential and low-lying basal terrain that conduces to the collection of surrounding waters. Basal mass increases in RIS region arise from subglacial lake water accretion and discharging
315 into the bedrock trench underneath the Recovery Glaciers (Bell et al., 2007), and similar basal mass increases might also occur in SG region. In DML region, basal mass increases occur in basal ridge, which might be attributed to the basal supercooling

condition in DML that conduce to the basal meltwater refreezing in basal ridge when flowing upward driven by basal hydraulic gradient. The possibility of basal water flowing upward to basal ridges has been verified in Gamburtsev Subglacial Mountain (GSM) through analysing a comprehensive geophysical data set (Creyts et al., 2014), and the consistent pattern is also shown

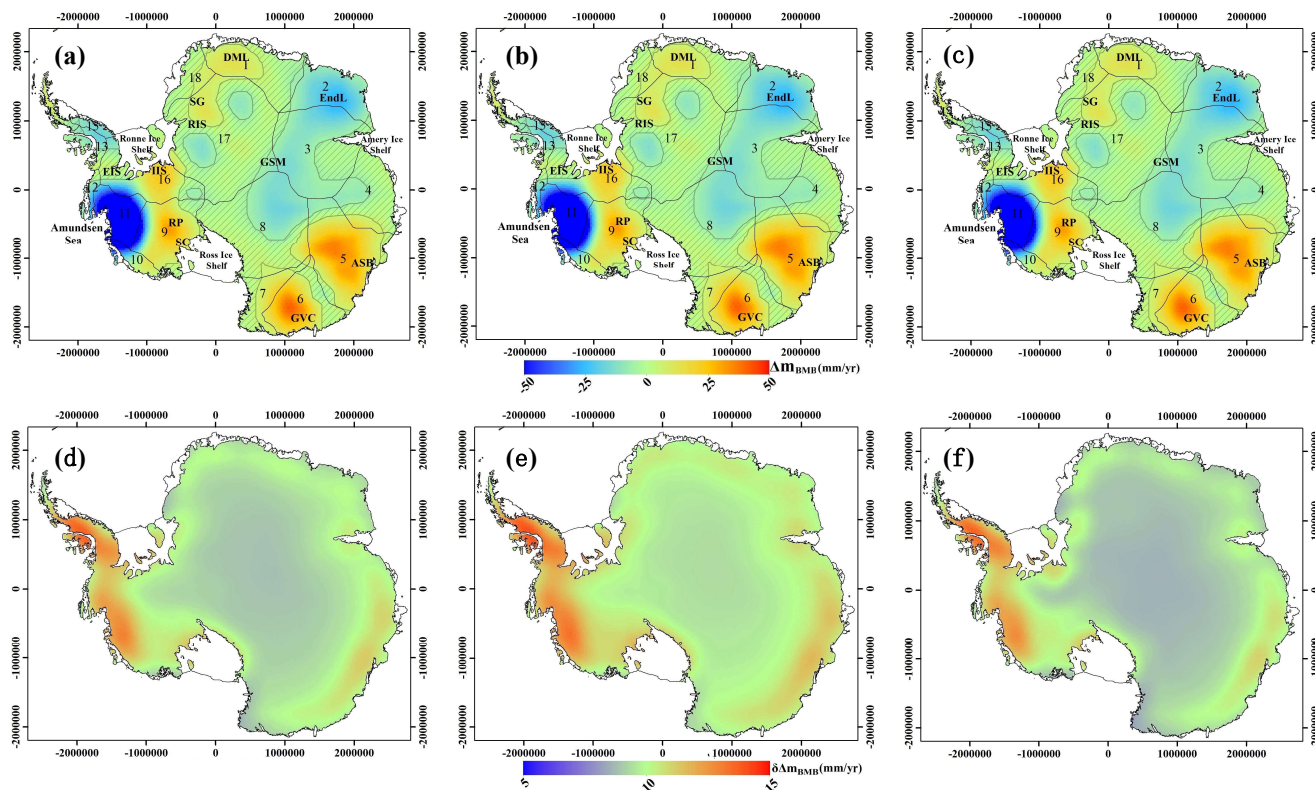320   in our BMB result, although the pattern is not significant enough in GSM region.

Figure 10 Basal mass balance (BMB) rates related to **(a)** ICE-6G, **(b)** IJ05_R2 and **(c)** W12a in unit of mm/yr, and **(d) (e) (f)**

associated standard deviations during 2003-2009. AIS drainage basins in **(a) (b) (c)** are determined according to the definitions of

Rignot et al. (2019), and the shaded area are regions where the BMB rates less than the associated standard deviations.

SC = Siple Coast; DML = Dronning Maud Land; EndL = Enderby Land; ASB = Aurora Subglacial Basin;

IIS = Institute Ice Stream; GVC = George V Coast; RIS = Recovery Ice Stream;

SG = Slessor Glacier; RP = Rockefeller Plateau; GSM = Gamburtsev Subglacial Mountain

Significant basal mass decreases occur mainly in Amundsen Sea coast, the interior of EAIS and Enderby Land (EndL) region. Among them, the most significant basal mass decreases along Amundsen Sea coast region are caused by the active ice melting in response to basal geothermal flux (Schroeder et al., 2014), this lead to a majority of basal water discharging into Amundsen Sea through basal channels (Gray et al., 2005). Basal mass decreases in the interior of EAIS are caused by the basal meltwater

325   generated from basal pressure-melting (Augustin et al., 2007) flows to marginal regions, driven by basal hydraulic potential gradient (Göeller, 2014). The decreases in EndL region lacks justification, which might also be caused by the volume scattering

in satellite altimetry data that underestimate surface height variation, or caused by the error in FDM that lead to the underestimation in surface mass loss in gravity forward modelling process, thereby impeding BMB estimation in these regions, and verifying these possible conjectures need further effort.

4.2 Basal water storage variations beneath Antarctic ice sheet

Antarctic basal water storage variations (BWSV) were estimated based on BMB and Antarctic basal melting rate data, through the combination method in section 2.2. It reveals mass variations of liquid water storage beneath Antarctic ice sheet. Table 2 displays regional BWSV rates related to 3 GIA models and associated standard deviations. As shown in Table 2, regional BWSV rates related to different GIA models also show similar values in each drainage basin: 2 drainage basins (B5 and B6) exhibit obvious basal water increases, and 1 drainage basin (B11) displays significant basal water decreases. Mean BWSV (average of BWSV rates related to 3 GIA models) rates in EAIS, WAIS are 47 ± 12 Gt/yr and -4 ± 5 Gt/yr, and no obvious BWSV occurs in APIS. The total mean BWSV rate beneath AIS is 43 ± 13 Gt/yr, accounting for 66% of the basal melting rate (65Gt/yr) (Pattyn, 2010), which indicates most of the basal melted water is stored in ice-bed interface.

Table 2 Regional Antarctic basal water storage variations (BWSV) rates and associated standard deviations related to 3 GIA models in 18 drainage basins, in unit of Gt/yr

Basin	BWSV(ICE-6G)		BWSV(IJ05_R2)		BWSV(W12a)		Basin	BWSV(ICE-6G)		BWSV(IJ05_R2)		BWSV(W12a)	
	Rates	Std	Rates	Std	Rates	Std		Rates	Std	Rates	Std	Rates	Std
B1	5	4	4	5	4	4	B11	-16	4	-15	4	-15	4
B2	-1	4	-2	4	-1	3	B12	0	1	0	1	0	1
B3	-2	8	-2	9	-2	7	B13	0	1	0	1	0	1
B4	4	5	4	5	4	4	B14	0	1	0	1	0	1
B5	17	7	18	8	15	7	B15	0	1	0	1	0	1
B6	11	4	11	5	10	4	B16	0	5	4	5	2	5
B7	4	2	4	2	4	2	B17	6	12	6	14	7	11
B8	2	9	1	10	3	8	B18	2	2	2	2	2	2
B9	6	5	13	6	10	5							
B10	0	1	0	1	0	1	Total	38	22	48	25	43	21

Figure 11a-11f displays the spatial distributions of BWSV rates on AIS related to 3 GIA models, and associated uncertainties, in form of equivalent water height (EWH). Where red colours represent basal water increases that arise from basal water migration and basal melting; blue colours represent basal water decreases that caused by basal water runoff or basal water refreezing; blue dots represent locations of active subglacial lakes that observed through surface height variations (Smith et al., 2009), grey dots are locations of definite or fuzzy subglacial lakes that detected by radio-echo sounding (RES) measurement

(Andrew and Martin, 2012). The spatial distributions of BWSV shown in Figure 11a-11c is similar to that of BMB in Figure 10a-10c, and the difference situated mainly in marginal regions of EAIS, where basal water increases are more extensive.

Results also show similar spatial distributions between obvious basal water increases (with the BWSV rates greater than associated standard deviations) and active subglacial lakes (blue circles in Figure 11a), such as the active subglacial lakes in

350   IIS, RP, GVC, ASB and SG regions. This indicates that the basal water volumes in most active subglacial lakes are increasing, despite water drainage occurs frequently; among them, the most typical justification is available in RP region, where the continued surface height increases in most subglacial lakes are found (Siegfried and Fricker, 2018). Definite or fuzzy lakes (grey circles in Figure 11b) are distributed mainly in regions of EA with low BWSV rates, exceptions are Concordia Subglacial lakes in Dome C (DC) where the basal water volumes are obviously increasing, this is attributed to the enhanced basal melting

355   in Concordia Ridge, Concordia Subglacial Lakes and Vincennes Basin regions that conduce to the replenishment of basal water storage (Carter, 2007).
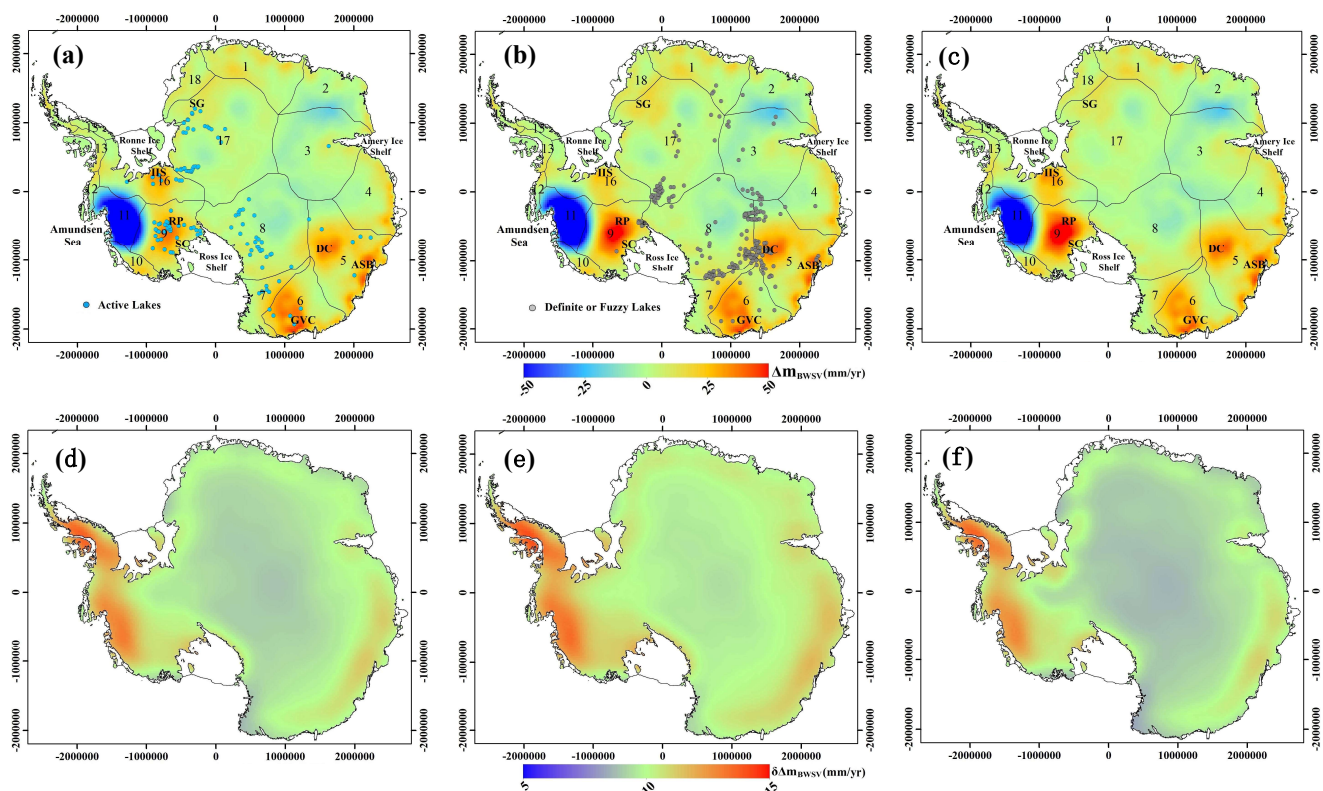

Figure 11 Basal water storage variations (BWSV) rates related to **(a)** ICE-6G, **(b)** IJ05_R2 and **(c)** W12a in unit of mm/yr, and **(d)** **(e)** **(f)** associated standard deviations during 2003-2009. Blue dots represent the location of active subglacial lakes observed by altimetry method, and grey dots represent the location of definite or fuzzy subglacial lakes detected by RES method. AIS drainage basins are determined according to the definitions of Rignot et al. (2019). DC = Dome C.

In most regions of AIS, obvious basal water increases appear at regions with rapid ice flows, such as Bindschadler, MacAyeal and Whillans ice streams in SC region, Ninnis and Mertz ice streams in GVC region, Totten ice stream in ASB region and Institute ice streams in IIS region. Table 3 listed the locations, names and velocities of some fast ice streams over AIS, and

360   corresponding basal water variations estimated in this study. Among them, most flow velocities are increasing during the study period. For example, flow velocities of Bindschadler and MacAyeal ice streams were accelerating during 2001-2014, which is attributed to the instability in the subglacial till and subglacial water flow (Hulbe et al., 2016); the acceleration of Ninnis and Mertz ice streams arise from the enhanced basal slip (Rignot et al., 2011); flow velocity of Totten ice stream had increased by 18% during 2000-2007 (Li et al., 2016). Regions without obvious basal water variations display no obvious flow velocity

365   increases, such as flow velocities in Rutford ice stream (Gudmundsson and Jenkins, 2009) in WA, and Fischer, Mellor and Lambert ice streams along Amery ice shelf. The spatial distribution relations between obvious basal water increases and rapid/accelerated flow velocities in most regions of AIS indicates that the accumulated basal water contribute to lubricating ice-rock interface and promote the ice flow above. However, exceptional cases are situated along Amundsen Sea coast (Pine Island and Thwaites glaciers), where significant basal water decreases follow rapid/accelerated ice flow (Han et al., 2016;Kim

370   et al., 2015). In these exceptional cases, rapid/accelerated flows arise from the combined effect of high basal geothermal flux induced basal ice-rock meltwater lubrication (Gray et al., 2005;Schroeder et al., 2014), as well as the buttressing loss induced by the extension of the shear zone and progressive disintegration (Kim et al., 2015). In summary, we believe that in most regions of AIS (except the Amundsen Sea coast), basal water storage variations appear to have an important effect on ice flow, except for other factors such as the stiffness of ice shelf, and flow velocities will further accelerate if basal water continues to

375   increase in these regions.

The Cryosphere
Discussions
Open Access
EGU

Table 3 Locations, names and flow variations of over AIS and corresponding BWSV. Columns give (1) locations of ice stream that shown in Figure 11; (2) ice stream names; (3) flow velocities, R donate rapid ice flows, S donate slow ice flows less than 500m/yr; (4) flow variations, ↑/N/↓ donate accelerated/steaty/slowed down flow; (5) basal water storage variations, ↑/N/↓ donate obvious increased/steady/decreased basal water storage; (6) reference.

Locations	Names	Flow velocities	Flow variations	BWSV	Reference
SC	Bindschadler	R	↑	↑	(Hulbe et al., 2016)
	MacAyeal	R	↑	↑	
	Whillans	R	↓	↑	(Winberry et al., 2014)
GVC	Ninnis	R	↑	↑	(Rignot et al., 2011)
	Mertz	R	↑	↑	
ASB	Totten	R	↑	↑	(Li et al., 2016)
Along Amery ice shelf	Fischer Mellor Lambert	R	N	N	(Pittard et al., 2015)
WA	Rutford	R	N	N	(Gudmundsson and Jenkins, 2009)
IIS	Institute	R	⊗	↑	(Rignot et al., 2011)
Amundsen Sea coast	Pine Island	R	↑	↓	(Han et al., 2016);
	Thwaites	R	↑	↓	(Kim et al., 2015);

5. Conclusions

In this study, we presented a layered gravity density forward/inversion method for estimating basal mass balance (BMB) and basal water storage variations (BWSV) rates beneath AIS during 2003-2009, by a combination of multi-source satellite observation data including satellite gravity, altimetry and GPS data, and relevant models including firn densification model (FDM), glacial isostatic adjustment and basal melting rate. The presented method used an iteration approach for separating gravity components caused by surface firn process and ice flow from the integrated gravity variations, to obtain the gravity variations and mass changes caused by BMB. When estimating BMB rates, 3 monthly GRACE gravity field solutions (CSR, GFZ and JPL), 3 inter-campaign biases corrections and 3 GIA models were used to obtain the average gravity variations, height variations and Earth's isostatic adjustment, to reduce possible errors.

Results reveal obvious spatial variability of BMB during 2003-2009, showing the potential for detecting BMB rates beneath AIS through the layered gravity density forward/inversion method. Significant basal mass decreases located mainly along Amundsen Sea coast, the interior of EAIS and Enderby Land region, while basal mass increases situated mainly in Rockefeller

Plateau, Siple Coast, Institute Ice Stream regions and marginal of EAIS. Total BMB rates beneath AIS are decreasing with the mean rate of -21 ± 13 Gt/yr (EAIS: 11 ± 12 Gt/yr, WAIS+APIS: -32 ± 5 Gt/yr), accounting for 28% of the mass balance rate

395 (-76Gt/yr) from Shepherd et al. (2018); and this indicates that the basal water migration between basal drainage systems and oceans is non-negligible in estimating AIS mass changes. BWSV rates exhibit a similar spatial distribution as BMB, and the total BWSV rates are increasing with the rate of 43 ± 13 Gt/yr (EAIS: 47 ± 12 Gt/yr, WAIS+APIS: -4 ± 5 Gt/yr), which is attributed to the active basal melting rate that producing sufficient meltwater to replenish the basal meltwater loss, and the excessed meltwater is stored beneath AIS that bring about increase in basal meltwater storage. BWSV results also show similar

400 spatial distribution between significant basal water increases and active subglacial lakes, indicating that the basal water in most active subglacial lakes is increasing, despite water drainage occurring frequently. Basal water in most definite or fuzzy lakes is relatively stable, exceptions are Concordia Subglacial lakes where the basal water is obviously increasing. We also found the spatial distribution relations between obvious basal water increases and rapid/accelerated flow velocities in most of the AIS (except the Amundsen Sea coast region), which indicates that basal water storage variations appear to have an important

405 effect on ice flow, and flow velocities will further accelerate if basal water continues to increase in these regions.

The main errors in estimating BMB come from the uncertainty of GRACE, FDM and inter-campaign biases of altimetry data, especially the current results of different inter-campaign biases corrections remain large discrepancy. A more elaborate result is desirable if utilizing more reliable and higher spatial/temporal resolution data, which deserves further studies.

The Cryosphere
Discussions

Code/Data availability

BMB and BWSV data is available at https://github.com/Kangjingyu17/BMB-BWSV.git

Dataset used in this study is listed as follows table.

Data set	URL	last access
GRACE	ftp://isdcftp.gfz-potsdam.de/grace/Level-2/	30 August 2021
ICESat	https://nsidc.org/data/icesat/	30 August 2021
BEDMAP2	https://secure.antarctica.ac.uk/data/bedmap2/	30 August 2021
GPS	https://dep1doc.gfz-potsdam.de/documents/102	30 August 2021
ICE-6G	https://www.atmosp.physics.utoronto.ca/~peltier/data.php	30 August 2021
W12a	http://www.pippawhitehouse.com/	30 August 2021

Any other specific data and code of this study is available on request to the authors.

Author contributions

Kang and Lu conceived the research. Kang performed forward modelling and inversion calculation. Shi processed ICESat data. Kang, Li and Zhang collected the verification data. Kang, Lu and Li interpreted the Antarctic basal mass/water storage variation, Kang, Lu and Zhang wrote the manuscript. All authors read and commented on the manuscript.

Competing interests

The authors declare that they have no conflict of interests.

Acknowledgements

Financial support

The Cryosphere
Discussions

References

Alley, R. B.: Flow-law hypotheses for ice-sheet modeling, Journal of Glaciology, 38, 245-256,
430   http://dx.doi.org/10.1017/S0022143000003658, 1992.

Alley, R. B., Lawson, D. E., Evenson, E. B., et al.: Glaciohydraulic supercooling: a freeze-on mechanism to create stratified,
       debris-rich basal ice: II. Theory, Journal of Glaciology, 44, 563-569, http://dx.doi.org/10.1017/S0022143000002070, 1998.

Andrew, W., and Martin, S.: A fourth inventory of Antarctic subglacial lakes, Antarctic ence, 24, 659-664,
       http://dx.doi.org/10.1017/S095410201200048X, 2012.

435   Argus, D. F., Peltier, W. R., Drummond, R., et al.: The Antarctica component of postglacial rebound model ICE-6G_C (VM5a)
       based on GPS positioning, exposure age dating of ice thicknesses, and relative sea level histories, Geophysical Journal
       International, 1, http://dx.doi.org/10.1093/gji/ggu140, 2014.

Augustin, L., Motoyama, H., Wilhelms, F., et al.: Drilling comparison in 'warm ice'and drill design comparison, Annals of
       Glaciology, 47, 73-78, http://dx.doi.org/10.3189/172756407786857820, 2007.

440   Bell, and Robin, E.: The role of subglacial water in ice-sheet mass balance, Nature Geoscience, 1, 297-304,
       http://dx.doi.org/10.1038/ngeo186, 2008.

Bell, R. E., Studinger, M., Shuman, C. A., et al.: Large subglacial lakes in East Antarctica at the onset of fast-flowing ice
       streams, Nature, 445, 904-907, http://dx.doi.org/10.1038/nature05554, 2007.

Brenner, A. C., DiMarzio, J. R., and Zwally, H. J.: Precision and accuracy of satellite radar and laser altimeter data over the
445   continental ice sheets, Ieee Transactions on Geoscience and Remote Sensing, 45, 321-331,
       http://dx.doi.org/10.1109/tgrs.2006.887172, 2007.

Carter, S. P.: Radar-based subglacial lake classification in Antarctica, Geochemistry, Geophysics, Geosystems,
       http://dx.doi.org/10.1029/2006GC001408, 2007.

Carter, S. P., Fricker, H., and Siegfried, M.: Active lakes in Antarctica survive on a sedimentary substrate–Part 1: Theory, The
450   Cryosphere Discussions, 9, 2053-2099, http://dx.doi.org/10.5194/tcd-9-2053-2015, 2015.

Chen, J. L., Wilson, C. R., Tapley, B. D., et al.: GRACE detects coseismic and postseismic deformation from the Sumatra-
       Andaman earthquake, Geophysical Research Letters, 34, http://dx.doi.org/10.1029/2007gl030356, 2007.

Cheng, M. K., Tapley, B. D., and Ries, J. C.: Deceleration in the Earth's oblateness, Journal of Geophysical Research-Solid
       Earth, 118, 740-747, http://dx.doi.org/10.1002/jgrb.50058, 2013.

455   Creyts, T. T., Ferraccioli, F., Bell, R. E., et al.: Freezing of ridges and water networks preserves the Gamburtsev Subglacial
       Mountains for millions of years, Geophysical Research Letters, 41, 8114-8122, http://dx.doi.org/10.1002/2014gl061491,
       2014.

Fisher, A. T., Mankoff, K. D., Tulaczyk, S. M., et al.: High geothermal heat flux measured below the West Antarctic Ice Sheet,
       Science advances, 1, e1500093, http://dx.doi.org/10.1126/sciadv.1500093, 2015.

24

The Cryosphere
Discussions

Open Access

EGU

460   Flament, T., Berthier, E., and Rémy, F.: Cascading water underneath Wilkes Land, East Antarctic ice sheet, observed using altimetry and digital elevation models, The Cryosphere, 8, http://dx.doi.org/10.5194/tc-8-673-2014, 2014.

Fretwell, P., Pritchard, H. D., Vaughan, D. G., et al.: Bedmap2: Improved ice bed, surface and thickness datasets for Antarctica, Cryosphere, 7, 375-393, http://dx.doi.org/10.5194/tc-7-375-2013, 2013.

Fricker, H. A., Scambos, T., Bindschadler, R., et al.: An active subglacial water system in West Antarctica mapped from space,
465   Science, 315, 1544-1548, http://dx.doi.org/10.1126/science. 1136897, 2007.

Fricker, H. A., Siegfried, M. R., Carter, S. P., et al.: A decade of progress in observing and modelling Antarctic subglacial water systems, Philosophical Transactions of the Royal Society A: Mathematical, Physical and Engineering Sciences, 374, 20140294, http://dx.doi.org/10.1098/rsta.2014.0294, 2016.

Gao, C. C., Lu, Y., Zhang, Z. Z., et al.: Ice sheet mass balance in Antarctica measured by GRACE and its uncertainty, Chinese
470   Journal of Geophysics-Chinese Edition, 58, 780-792, http://dx.doi.org/10.6038/cjg20150308, 2015.

Göeller, S., Thoma, M., Grosfeld, K., et al.: A balanced water layer concept for subglacial hydrology in large scale ice sheet models, The Cryosphere Discussions, 6, 5225-5253, http://dx.doi.org/10.5194/tc-7-1095-2013, 2012.

Göeller, S.: Antarctic subglacial hydrology-interactions of subglacial lakes, basal water flow and ice dynamics, State and University Library of Bremen, 2014.

475   Gray, L., Joughin, I., Tulaczyk, S., et al.: Evidence for subglacial water transport in the West Antarctic Ice Sheet through three-dimensional satellite radar interferometry, Geophysical Research Letters, 32, http://dx.doi.org/10.1029/2004GL021387, 2005.

Gudmundsson, G. H., and Jenkins, A.: Ice-flow velocities on Rutford Ice Stream, West Antarctica, are stable over decadal timescales, Journal of Glaciology, 55, 339-344, http://dx.doi.org/10.3189/002214309788608697, 2009.

480   Gunter, B., Urban, T., Riva, R., et al.: A comparison of coincident GRACE and ICESat data over Antarctica, Journal of Geodesy, 83, http://dx.doi.org/10.1007/s00190-009-0323-4, 2009.

Gunter, B., Didova, O., Riva, R., et al.: Empirical estimation of present-day Antarctic glacial isostatic adjustment and ice mass change, The Cryosphere, 8, 743-760, http://dx.doi.org/10.5194/tc-8-743-2014, 2014.

Han, H., Im, J., and Kim, H. C.: Variations in ice velocities of Pine Island Glacier Ice Shelf evaluated using multispectral
485   image matching of Landsat time series data, Remote Sensing of Environment, 186, 358-371, http://dx.doi.org/10.1016/j.rse.2016.09.001, 2016.

Heiskanen, W. A., and Moritz, H.: Physical geodesy, Bulletin Gæodésique, 86, 491-492, 1967.

Hofmann-Wellenhof, B., and Moritz, H.: Physical geodesy, Springer Science & Business Media, 2006.

Hulbe, C. L., Scambos, T. A., Klinger, M., et al.: Flow variability and ongoing margin shifts on Bindschadler and MacAyeal
490   Ice Streams, West Antarctica, Journal of Geophysical Research-Earth Surface, 121, 283-293, http://dx.doi.org/10.1002/2015jf003670, 2016.

Ivins, E. R., James, T. S., Wahr, J., et al.: Antarctic contribution to sea level rise observed by GRACE with improved GIA correction, 2013.

Kaspers, K. A., Wal, R. S. W. V. D., Broeke, M. R. V. D., et al.: Model calculations of the age of firn air across the Antarctic
495   continent, Atmospheric Chemistry and Physics, 4, 2004.

Keenan, E., Wever, N., Dattler, M., et al.: Physics-based SNOWPACK model improves representation of near-surface
       Antarctic snow and firn density, Cryosphere, 15, 1065-1085, http://dx.doi.org/10.5194/tc-15-1065-2021, 2021.

Kim, J. W., Kim, D. J., Kim, S. H., et al.: Disintegration and acceleration of Thwaites Ice Shelf on the Amundsen Sea revealed
       from remote sensing measurements, Giscience & Remote Sensing, 52, 498-509,
500   http://dx.doi.org/10.1080/15481603.2015.1041766, 2015.

Li, X., Rignot, E., and Mouginot, J.: Ice flow dynamics and mass loss of Totten Glacier, East Antarctica, from 1989 to 2015,
       Geophysical Research Letters, 43, 6366-6373, http://dx.doi.org/10.1002/2016gl069173, 2016.

Liefferinge, B. V., Pattyn, F., Cavitte, M. G. P., et al.: Promising Oldest Ice sites in East Antarctica based on thermodynamical
       modelling, The Cryosphere Discussions, 12, 1-22, http://dx.doi.org/10.5194/tc-12-2773-2018, 2018.

505   Ligtenberg, S., Helsen, M., and Van den Broeke, M.: An improved semi-empirical model for the densification of Antarctic
       firn, The Cryosphere, 5, 809-819, http://dx.doi.org/10.5194/tc-5-809-2011, 2011.

Ligtenberg, S.: The present and future state of the Antarctic firn layer, Utrecht University, 2014.

Martos, Y. M., Catalán, M., Jordan, T. A., et al.: Heat flux distribution of Antarctica unveiled, Geophysical Research Letters,
       44, 11,417-411,426, http://dx.doi.org/10.1002/2017GL075609, 2017.

510   Pattyn, F.: Investigating the stability of subglacial lakes with a full Stokes ice-sheet model, Journal of Glaciology, 54, 353-
       361, http://dx.doi.org/10.3189/002214308784886171, 2008.

Pattyn, F.: Antarctic subglacial conditions inferred from a hybrid ice sheet/ice stream model, Earth and Planetary Science
       Letters, 295, 451-461, http://dx.doi.org/10.1016/j.epsl.2010.04.025, 2010.

Peltier, W., R., et al.: Space geodesy constrains ice age terminal deglaciation: The global ICE-6G_C (VM5a) model, Journal
515   of Geophysical Research Solid Earth Jgr, 2015.

Pittard, M. L., Roberts, J. L., Watson, C. S., et al.: Velocities of the Amery Ice Shelf's primary tributary glaciers, 2004-12,
       Antarctic Science, 27, 511-523, http://dx.doi.org/10.1017/s0954102015000231, 2015.

Richter, A., Popov, S. V., Fritsche, M., et al.: Height changes over subglacial Lake Vostok, East Antarctica: Insights from
       GNSS observations, Journal of Geophysical Research-Earth Surface, 119, 2460-2480,
520   http://dx.doi.org/10.1002/2014jf003228, 2014.

Rignot, E., and Jacobs, S. S.: Rapid Bottom Melting Widespread near Antarctic Ice Sheet Grounding Lines, Science, 296,
       2020-2023, http://dx.doi.org/10.1126/science.1070942, 2002.

Rignot, E., Mouginot, J., and Scheuchl, B.: Ice Flow of the Antarctic Ice Sheet, Science, 333, 1427-1430,
       http://dx.doi.org/10.1126/science.1208336, 2011.

525   Rignot, E., Mouginot, J., Scheuchl, B., et al.: Four decades of Antarctic Ice Sheet mass balance from 1979–2017, Proceedings
       of the National Academy of Sciences, 116, 1095-1103, http://dx.doi.org/10.1073/pnas.1812883116, 2019.

Sasgen, I., Martin, A., Horvath, A., et al.: Regional glacial-isostatic adjustment in Antarctica inferred from combining spaceborne geodetic observations (ESA-STSE CryoSat+ Project REGINA), EGU General Assembly Conference Abstracts, 2016,

530 Schroeder, D. M., Blankenship, D. D., Young, D. A., et al.: Evidence for elevated and spatially variable geothermal flux beneath the West Antarctic Ice Sheet, Proceedings of the National Academy of Sciences, 111, 9070-9072, http://dx.doi.org/10.1073/pnas.1405184111, 2014.

Schroeder, L., Horwath, M., Dietrich, R., et al.: Long Term Elevation Change of the Antarctic Ice Sheet from Multi-Mission Satellite Altimetry, Agu Fall Meeting, 2016,

535 Shepherd, A., Ivins, E., Rignot, E., et al.: Mass balance of the Antarctic Ice Sheet from 1992 to 2017, Nature, 558, 219-+, http://dx.doi.org/10.1038/s41586-018-0179-y, 2018.

Siegfried, M. R., and Fricker, H. A.: Thirteen years of subglacial lake activity in Antarctica from multi-mission satellite altimetry, Annals of Glaciology, 59, 42-55, http://dx.doi.org/10.1017/aog.2017.36, 2018.

Smith, B. E., Bentley, C. R., and Raymond, C. F.: Recent elevation changes on the ice streams and ridges of the Ross 540 Embayment from ICESat crossovers, Geophysical Research Letters, 32, http://dx.doi.org/10.1029/2005gl024365, 2005.

Smith, B. E., Fricker, H. A., Joughin, I. R., et al.: An inventory of active subglacial lakes in Antarctica detected by ICESat (2003-2008), Journal of Glaciology, 55, 573-595, http://dx.doi.org/10.3189/002214309789470879, 2009.

Swenson, S., Chambers, D., and Wahr, J.: Estimating geocenter variations from a combination of GRACE and ocean model output, Journal of Geophysical Research-Solid Earth, 113, http://dx.doi.org/10.1029/2007jb005338, 2008.

545 Van Liefferinge, B., and Pattyn, F.: Using ice-flow models to evaluate potential sites of million year-old ice in Antarctica, Clim. Past, 9, 2335-2345, http://dx.doi.org/10.5194/cp-9-2335-2013, 2013.

Wahr, J., Molenaar, M., and Bryan, F.: Time variability of the Earth's gravity field: Hydrological and oceanic effects and their possible detection using GRACE, Journal of Geophysical Research: Solid Earth, 103, 30205-30229, http://dx.doi.org/10.1029/98JB02844, 1998.

550 Wahr, J., Swenson, S., and Velicogna, I.: The accuracy of GRACE mass estimates, Geophysical Research Letters, 33, http://dx.doi.org/10.1029/2005GL025305, 2006.

Whitehouse, P. L., Bentley, M. J., Milne, G. A., et al.: A new glacial isostatic adjustment model for Antarctica: calibrated and tested using observations of relative sea-level change and present-day uplift rates, Geophysical Journal International, 190, 1464-1482, http://dx.doi.org/10.1111/j.1365-246X.2012.05557.x, 2012.

555 Winberry, J. P., Anandakrishnan, S., Alley, R. B., et al.: Tidal pacing, skipped slips and the slowdown of Whillans Ice Stream, Antarctica, Journal of Glaciology, 60, 795-807, http://dx.doi.org/10.3189/2014JoG14J038, 2014.

Wingham, D. J., Siegert, M. J., Shepherd, A., et al.: Rapid discharge connects Antarctic subglacial lakes, Nature, 440, 1033-1036, http://dx.doi.org/10.1038/nature04660, 2006.

Wright, A., Young, D. A., Roberts, J., et al.: Evidence of a hydrological connection between the ice divide and ice sheet margin in the Aurora Subglacial Basin, East Antarctica, Journal of Geophysical Research: Earth Surface, 117, http://dx.doi.org/10.1029/2011JF002066, 2012.

Young, D. A., Schroeder, D., Blankenship, D. D., et al.: The distribution of basal water between Antarctic subglacial lakes from radar sounding, Philosophical Transactions of the Royal Society A: Mathematical, Physical and Engineering Sciences, 374, 20140297, http://dx.doi.org/10.1098/rsta.2014.0297, 2016.

Zwally, H. J., Schutz, B., Abdalati, W., et al.: ICESat's laser measurements of polar ice, atmosphere, ocean, and land, Journal of Geodynamics, 34, 405-445, http://dx.doi.org/10.1016/s0264-3707(02)00042-x, 2002.

Zwally, H. J., Giovinetto, M. B., Li, J., et al.: Mass changes of the Greenland and Antarctic ice sheets and shelves and contributions to sea-level rise: 1992-2002, Journal of Glaciology, 51, 509-527, http://dx.doi.org/10.3189/172756505781829007, 2005.

Zwally, H. J., Li, J., Robbins, J. W., et al.: Mass gains of the Antarctic ice sheet exceed losses, Journal of Glaciology, 61, 1019-1036, http://dx.doi.org/10.3189/2015JoG15J071, 2015.